# Regelungs- und Schutzaspekte für doppeltgespeiste Asynchrongeneratoren in Windkraftanlagen

--

## Control and Protection Aspects for Doubly Fed Induction Generators in Wind Energy Systems

C. Andrei

M.B.C. Salles

K. Hameyer

Institute of Electrical Machines (IEM)

RWTH Aachen University

# Inhaltsverzeichnis / Contents

# 1  Abstract

Due to the development of the wind energy market and its high penetration in the power sector, wind turbines have to satisfy stricter grid code requirements in order to guarantee a reliable operation of the power system. According to these grid codes, wind turbines must remain connected and also inject reactive power into the grid during grid faults and after their elimination. Different control strategies and protection systems for Doubly Fed Induction Generator (DFIG) based wind turbines during grid faults are proposed in this paper. The influences of such protection systems on the performance of the wind turbines are studied. Aspects of shaft voltage and bearing currents are also presented.

# 2  Introduction

With regard to the rapidly increasing lack of conventional energy sources, the public interest has been focused towards renewable and reliable energy resources worldwide. The wind energy sector is one of the most important markets.

This paper presents various control and protection strategies for the DFIG based wind turbines during grid faults (sections 3 to 4), as well as giving a brief overview of different aspects regarding shaft voltages and the resulting bearing currents in DFIG (section 5). A concluding summary of the discussed points is presented in section 6.

# 3  Wind Turbine Model Based on Doubly Fed Induction Generators (DFIG)

The implementation of the DFIG wind turbine dynamic model was based on the MATLAB/Simulink SimPowerSystems toolbox. The generator model is described by an one mass shaft representation.

## 3.1  Aerodynamic Model

The mechanical power that can be captured from the wind through the wind turbine rotor and the mechanical torque developed by the turbine can be determined using the well-known aerodynamic equations (1) and (2) [SLOO03, AKHM03]:

$$P_m = \frac{1}{2} \cdot A \cdot \rho \cdot V^3 \cdot C_p(\lambda, \beta) \tag{1}$$

$$T_m = \frac{P_m}{\omega_m} = \frac{1}{2} \cdot A \cdot \rho \cdot V^2 \cdot C_p(\lambda, \beta) \cdot \frac{R}{\lambda} \tag{2}$$

where $T_m$ ($N \cdot m$) is the mechanical torque, $P_m$ ($W$) is the mechanical power, $A$ ($m^2$) is the area of the wind turbine rotor, $R$ ($m$) is the radius of the wind turbine rotor, $\rho$ ($kg/m^3$) is the air density, $V$ ($m/s$) is the wind speed, $C_p$ is the power coefficient (also known as performance coefficient), $\lambda = \omega_m \cdot R/V$ is the tip speed ratio, $\omega_m$ ($rad/s$) is the angular speed of the wind turbine and $\beta$ (°) is the blade pitch angle.

The power coefficient ($C_p$) defines to which extent the wind turbine can capture the energy from the wind and convert it into rotational mechanical power through its rotor blades. The maximum theoretic value that $C_p$ can reach is given by the Betz limit of 0.59 [AKHM03]. For the implemented wind turbine model, (3) and (4) were used to determine the required $C_p$ characteristics. The coefficients $c_1 - c_9$, indicated in Table 1, were suggested for a better reflection of the aerodynamics of modern wind turbines [SLOO03].

$$C_p(\lambda, \beta) = c_1 \cdot \left( \frac{c_2}{\lambda_i} - c_3 \cdot \beta - c_4 \cdot \beta^{c_5} - c_6 \right) \cdot e^{-\frac{c_7}{\lambda_i}} \tag{3}$$

$$\lambda_i = \frac{1}{\dfrac{1}{\lambda + c_8 \cdot \beta} - \dfrac{c_9}{\beta^3 + 1}} \tag{4}$$

| $c_1$ | $c_2$ | $c_3$ | $c_4$ | $c_5$ | $c_6$ | $c_7$ | $c_8$ | $c_9$ |
|-------|-------|-------|-------|-------|-------|-------|-------|-------|
| 0.73 | 151 | 0.58 | 0.002 | 2.14 | 13.2 | 18.4 | -0.02 | -0.003 |

**Table 1:** Optimized values for the $C_p$ equation coefficients [SLOO03].

Figure 1 shows the $C_p$ characteristics suggested in [SLOO03] for the dynamic analysis of wind turbines, calculated for different values of the tip speed ratio $\lambda$ and of the blade pitch angle $\beta$.
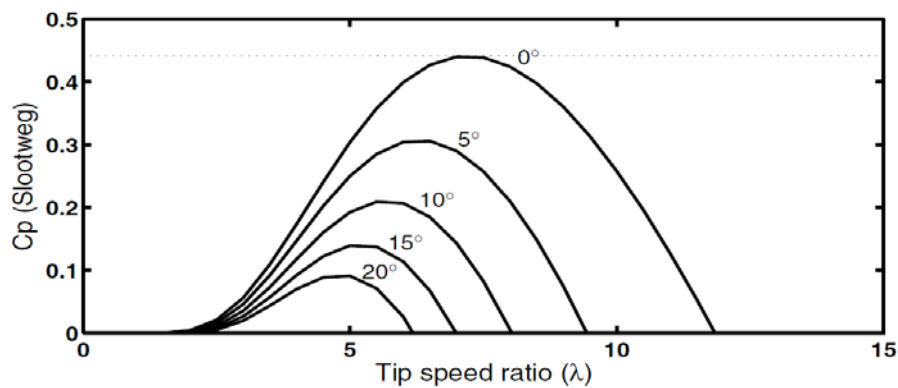
**Figure 1:** $C_p$ characteristics for different tip speed ratios $\lambda$ and blade pitch angle positions $\beta$ [SLOO03].

## 3.2 Electrical Model and Control of the DFIG Converters

Wind turbines with DFIG are a very common configuration of wind turbines in today's wind energy systems. The generator's concept of a rotor fed system together with the development of highly efficient power electronics offers the possibility of supersynchronous, as well as subsynchronous operation, which provides an advantageous „speed elasticity". Figure 2 schematically illustrates the concept of a DFIG based wind energy system. The stator is directly grid connected, whereas the rotor windings are connected to the grid via two back-to-back voltage source converters.

The basic operation of the two converters can be summarized as follows: the grid-side converter (GSC) controls the active power flow between the rotor windings and the grid, depending on the point of operation. Active power is either being injected into the grid in supersynchronous mode (slip $s > 0$) or respectively absorbed by the rotor windings in subsynchronous mode ($s < 0$). The rotor-side converter (RSC) determines the rotor speed and regulates the injection of reactive power into the grid through the rotor windings, in order to maintain a unitary power factor operation of the wind energy system. This variable speed operation allows to maximize the power coefficient ($C_p$) during operation of the wind turbine for different wind speeds.
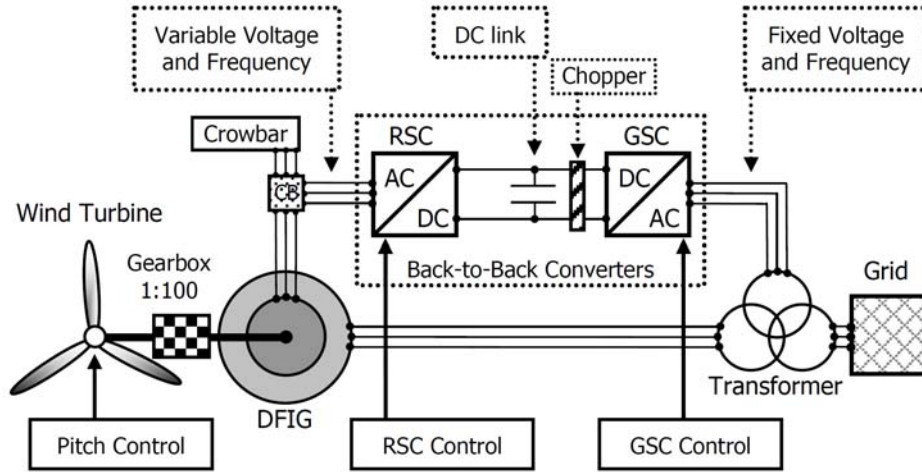
**Figure 2:** Diagram of a Doubly Fed Induction Generator (DFIG) based wind energy system [SALL10].

### 3.2.1 Control of the Rotor-Side Converter (RSC) in Normal Operation

The RSC controls the reactive power ($Q$) injection and the developed electric power ($P_{elec}$) by the DFIG, as shown in Figure 3. The electric power reference ($P^*_{opt}$) is determined based on the optimum rotor speed given by the $C_p$ characteristic in Figure 1, depending on the wind speed as parameter. An encoder delivers the rotor speed ($\theta$) of the generator required by the $abc-dq0$ and the $dq0-abc$ transformations, in order to simplify the three-phase currents and voltages into direct-quadrature components.

The direct axis component of the current ($I_d$) regulates the power factor of the generator to $1\,pu$ (per unit), thus setting the reactive power reference ($Q^*$) to be equal to zero. The actual absorbed reactive power of the DFIG ($Q$) is compared to the reference. The reference direct axis current ($I^*_d$) is then calculated from the resulting error, through a PI controller. Next the $I^*_d$ is compared to the actual direct axis current ($I_d$), and the error is then sent to another PI controller to determine the reference of the direct axis voltage ($V^*_d$).

The quadrature axis component of the current ($I^*_q$), controlled in a similar manner as the direct axis component, regulates the developed electric power ($P_{elec}$) to an optimal reference ($P^*_{opt}$). The direct-quadrature components of the reference voltages ($V^*_d$ and $V^*_q$) are then transformed back into three-phase voltages ($V^*_{abc\_rsc}$), required at the RSC output, through a $dq0-abc$ transformation. The converters IGBT's are considered to be ideal and commutation losses are therefore neglected.
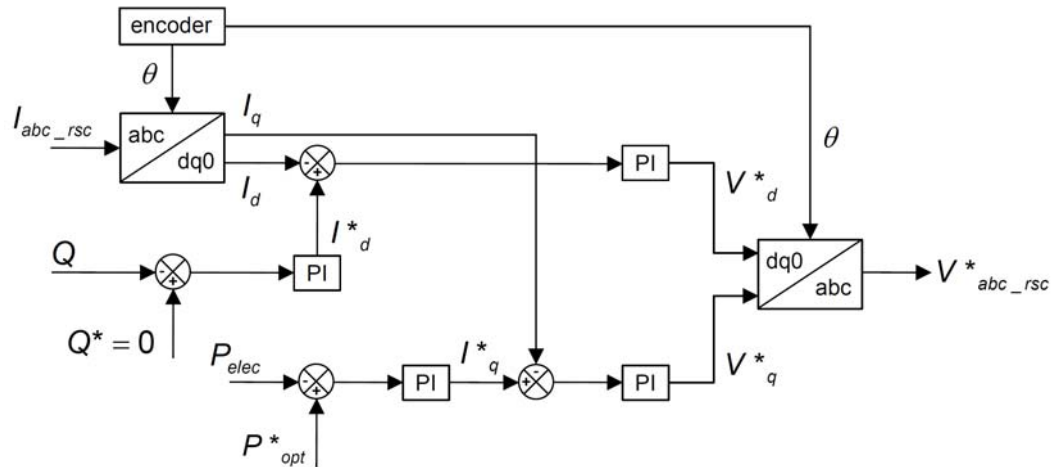
**Figure 3:** Normal Operation Control Diagram of the Rotor-Side Converter [SALL08].

### 3.2.2 Control of the Grid-Side Converter (GSC) in Normal Operation

The GSC controls the voltage level at the direct-current link (DC link) between the two converters (Figure 2). A PLL (Phase Locked Loop) provides the angle ($\phi$) needed by the $abc-dq0$ and the $dq0-abc$ transformations to synchronize the three-phase voltages at the converters output with the zero crossings fundamental component of the phase $A$ grid voltage. A control diagram for the GSC is shown in Figure 4.
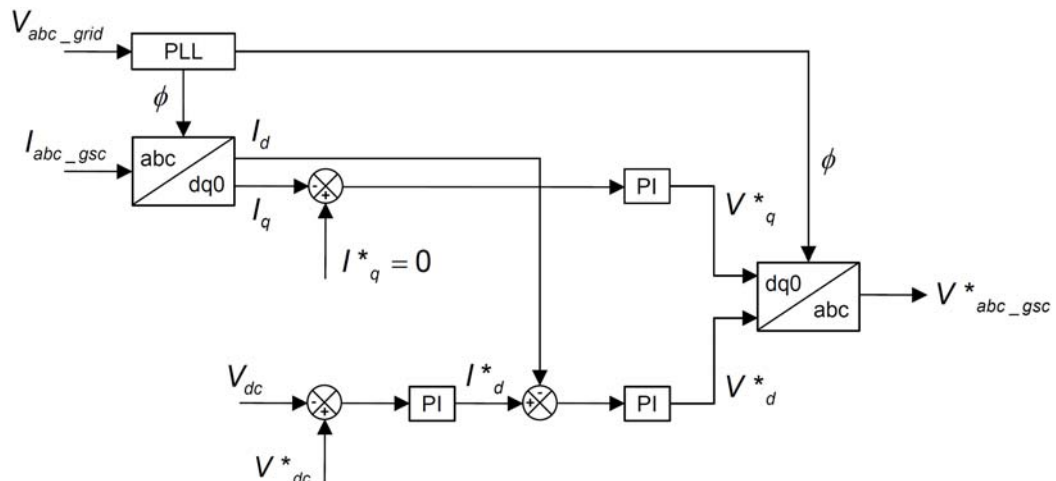


**Figure 4:** Normal Operation Control Diagram of the Grid-Side Converter [SALL08].

The DC link reference voltage level ($V^*_{dc}$) is set to $1\,pu$ by the direct axis component. This reference voltage is compared to the actual voltage and from the resulting error the direct axis component of the reference current ($I^*_d$) is being calculated through a

PI controller. $I^*_d$ is then compared to the actual value of the direct axis current ($I_d$) and then sent to another PI controller, in order to calculate the direct axis reference voltage ($V^*_d$).

There is no need for a GSC reactive power regulation, since the RSC already controls the power factor of the DFIG. Therefore the quadrature axis component of the reference current is set to zero ($I^*_q = 0$). $I^*_q$ is then compared to the quadrature axis component of the actual current ($I_q$) and the error is sent to a PI controller to determine the quadrature axis component of the reference voltage ($V^*_q$). The two components of the reference voltage ($V^*_d$ and $V^*_q$) are then transformed into the three-phase voltages ($V^*_{abc\_gsc}$) needed at the output of the GSC.

## 3.3 DFIG Protection by the Crowbar System

In the schematic diagram shown in Figure 2, the RSC is connected to the rotor windings of the DFIG through a protection system, commonly known as crowbar system. The role of the crowbar system is to disconnect the rotor windings of the DFIG during grid faults, mainly short circuits that occur in the vicinity of the wind energy system. Such faults can lead to over-currents in the rotor windings or over-voltages in the DC-link, due to the fact that the stator windings are directly grid-connected. Also, the back-to-back converter connecting the rotor windings to the grid is very sensitive to over-currents. In these cases the crowbar system is activated. In modern wind energy systems the crowbar system is based on a three-phase serially connected resistance, which is controlled by power electronic circuits. The crowbar system is activated and deactivated in four steps:

- The rotor windings of the DFIG are disconnected from the RSC (with the help of circuit breakers – CB, see Figure 2).

- The three-phase resistance is serially connected to the rotor windings (the crowbar system).

- The crowbar system is disconnected from the rotor windings.

- The RSC is reconnected to the rotor windings.

In order to balance the difference between the active electrical power injected into the power system by the GSC and the active electrical power injected into the DC-link by the RSC, a DC-chopper is added (see Figure 2). The DC-chopper is a thyristor controlled resistance, which dissipates the unbalance of electrical power during grid faults [SALL10]. More detailed information regarding the protection of wind energy systems through crowbar systems can be found in [AKHM03, SEMA06].

# 4 Dynamic Analysis of DFIG in Wind Energy Systems

The test system used for the dynamic analysis is a modified version of the well-known Western System Coordinated Council (WSCC-9) Bus System [SAUE98]. The system, shown in Figure 5, is composed of nine buses (six at 230 *kV*, one at 16.5 *kV*, one at 18 *kV* and one at 13.8 *kV*), nine branches, three loads and three generators, representing a swing bus, a 100 *MVA* synchronous generator and a 164 *MW* wind farm.
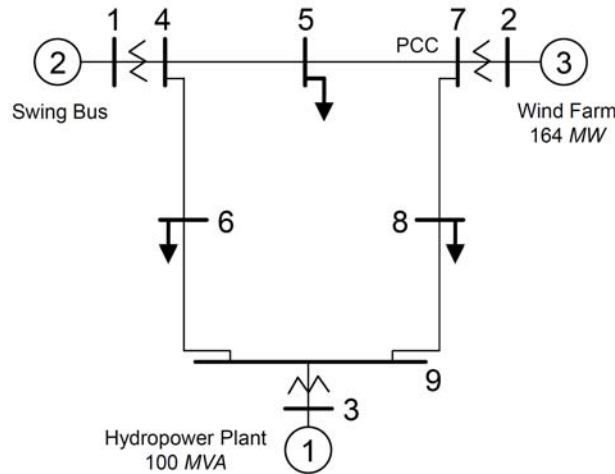


**Figure 5:** Diagram of the modified WSCC-9 Bus System [SALL10].

The investigated analysis is performed for two grid faults in the WSCC-9 Bus System, one at Bus 5 and another at Bus 7, both with a duration of 150 *ms.*

## 4.1 Converter Control Strategies during Grid Faults

In this section three different control strategies of the DFIG converters during grid faults are studied. These control strategies enable the injection of reactive power into the grid during faults and also regulate the DC-link voltage levels. They can be briefly summarized as follows [SALL09]:

- Case A: The RSC and the GSC work as in normal operation; the RSC control is switched from constant power factor to constant voltage.

- Case B: The RSC works in the same way as in Case A; the GSC controls the voltage level at the DC-link, as in normal operation, and the reactive power flow.

- Case C: The RSC regulates the optimum active electrical power, while the power factor control is deactivated; the GSC control is the same as in Case B.

### 4.1.1 Fault at Bus 5 Cleared After 150 *ms*

For this scenario, Figures 6 – 8 illustrate the terminal voltage level, the DC-link voltage level and the reactive power level for all three control strategies mentioned above [SALL09].
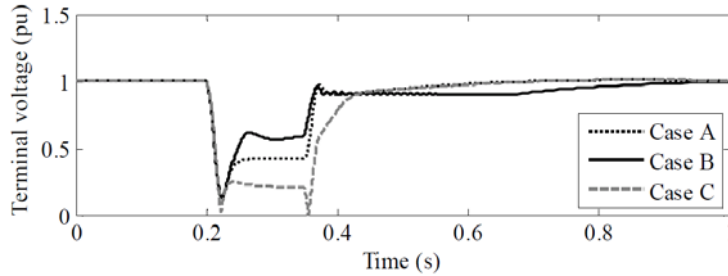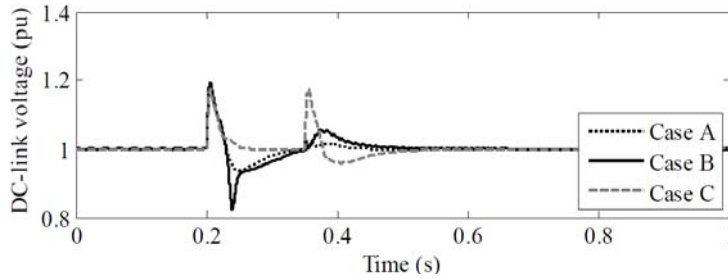


**Figure 6:** Terminal voltage level.



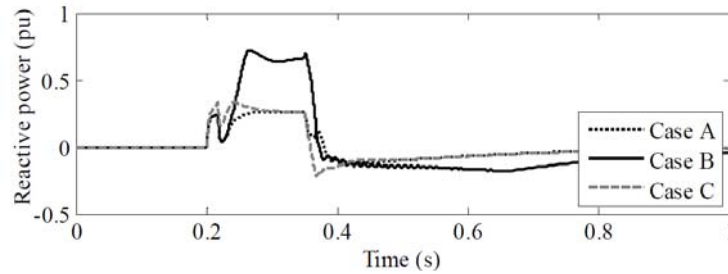**Figure 7:** DC-link voltage level.



**Figure 8:** Reactive power level.

The terminal voltage has the highest level in Case B (Figure 6), due to the RSC control of the terminal voltage and additional reactive power injection by the GSC (Figure 8). The lowest terminal voltage level corresponds to Case C, because the RSC does not participate in controlling the reactive power flow. The DC-link voltage levels are kept in acceptable limits in all three control strategies (Figure 7), but Case C shows a second transient [SALL09].

### 4.1.2 Fault at Bus 7 Cleared After 150 *ms*

Figures 9 – 11 indicate the terminal voltage, the DC-link voltage and the reactive power characteristics for the three investigated control strategies [SALL09].
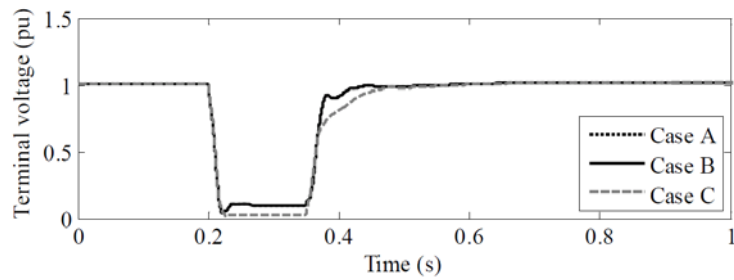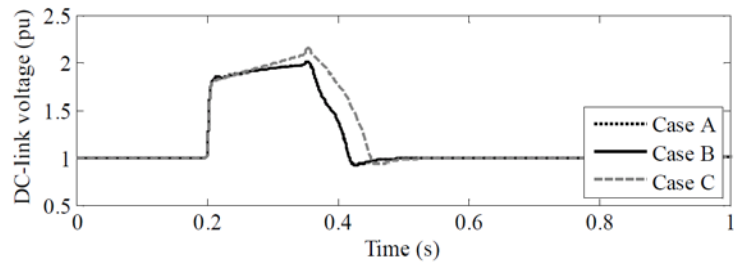
**Figure 9:** Terminal voltage level.



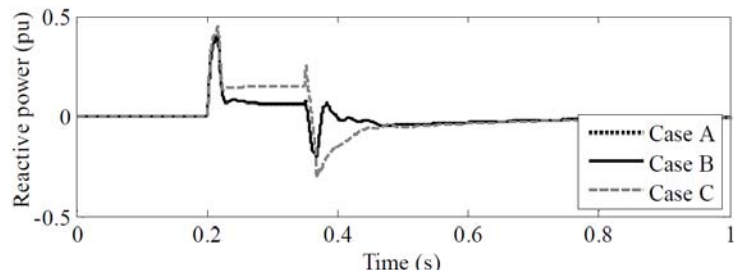**Figure 10:** DC-link voltage level.



**Figure 11:** Reactive power level.

In this scenario, the grid fault occurs at the PCC at Bus 7. The terminal voltages have low values, which limits the injection of active and reactive power. The control strategy used in Case B displays the highest terminal voltage level (Figure 9), as well as the lowest consumption of reactive power (Figure 11). The DC-link voltage levels have reached 2 *pu* in all three cases (Figure 10), exceeding the acceptable limits and thus indicating that the DFIG can not remain grid-connected during severe grid faults, without the use of some protection systems, such as for instance the crowbar system (please refer to the next section) [SALL09].

## 4.2 Crowbar System Activation during Grid Faults

This paragraph describes the influences of the resistance value and operation time of the crowbar system on the dynamic performance of DFIG based wind energy systems, for the same fault scenarios considered in the previous section.

### 4.2.1 Influence of the Resistance Value of the Crowbar System

The protection strategy implemented for this analysis during a grid fault is as follows: first the RSC is blocked and the crowbar system is activated, whereby the DC-link voltage is regulated by the GSC; then the RSC is restarted and the crowbar system is deactivated, once the fault has been eliminated. This strategy is common in countries where no reactive power injection is required.
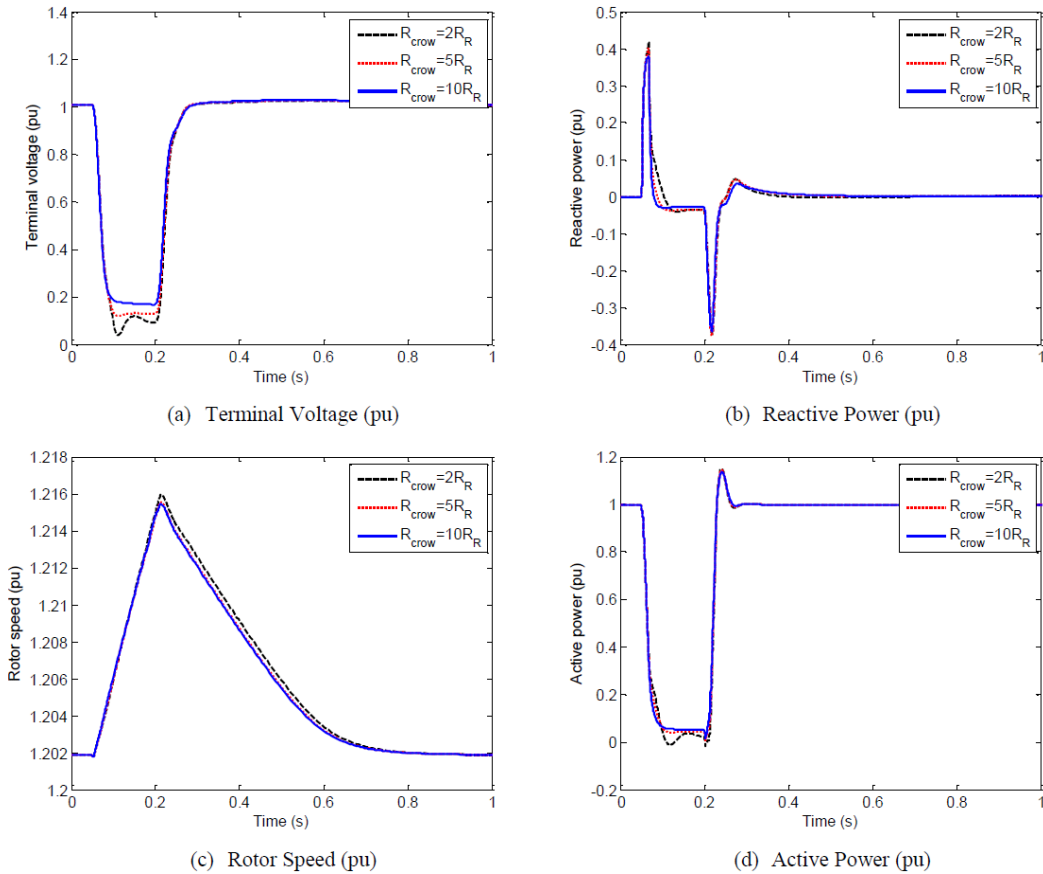


(a)  Terminal Voltage (pu)  (b)  Reactive Power (pu)

(c)  Rotor Speed (pu)  (d)  Active Power (pu)

**Figure 12:** Dynamic analysis of the DFIG for different resistance values of the crowbar system, during a 150 *ms* fault at Bus 5 [SALL10].

Figure 12 shows the characteristics of different parameters for three values of the crowbar system's resistance $R_{crow}$ (2, 5 and 10 times the resistance of the DFIG rotor $R_R$), in the case of a fault occurring at Bus 5 and eliminated after 150 *ms*.

The highest terminal voltage level is for $R_{crow} = 10 \cdot R_R$ (Figure 12a). The rotor speed decreases (Figure 12c), due to the low consumption of reactive power during the fault (Figure 12b). The desired rotor speed should be as close to the normal operation speed as possible, in order to avoid the critical rotor speed affecting the machine's stability. More active power is also injected for higher values of the crowbar system resistance (Figure 12d) [SALL10].

For a grid fault occurring close to the wind farm's terminals (at Bus 7), the dynamic analysis is illustrated by the characteristics in Figure 13. There are no significant differences between the three given resistance values. The crowbar system is still necessary for a fast reconnection of the RSC and for the protection of its power electronics. If the fault is not eliminated before reaching the critical rotor speed, the machine's operation can become unstable [SALL10]. The timeframe in which the wind energy systems have to remain grid-connected is given by the regional Transmission System Operator (TSO).
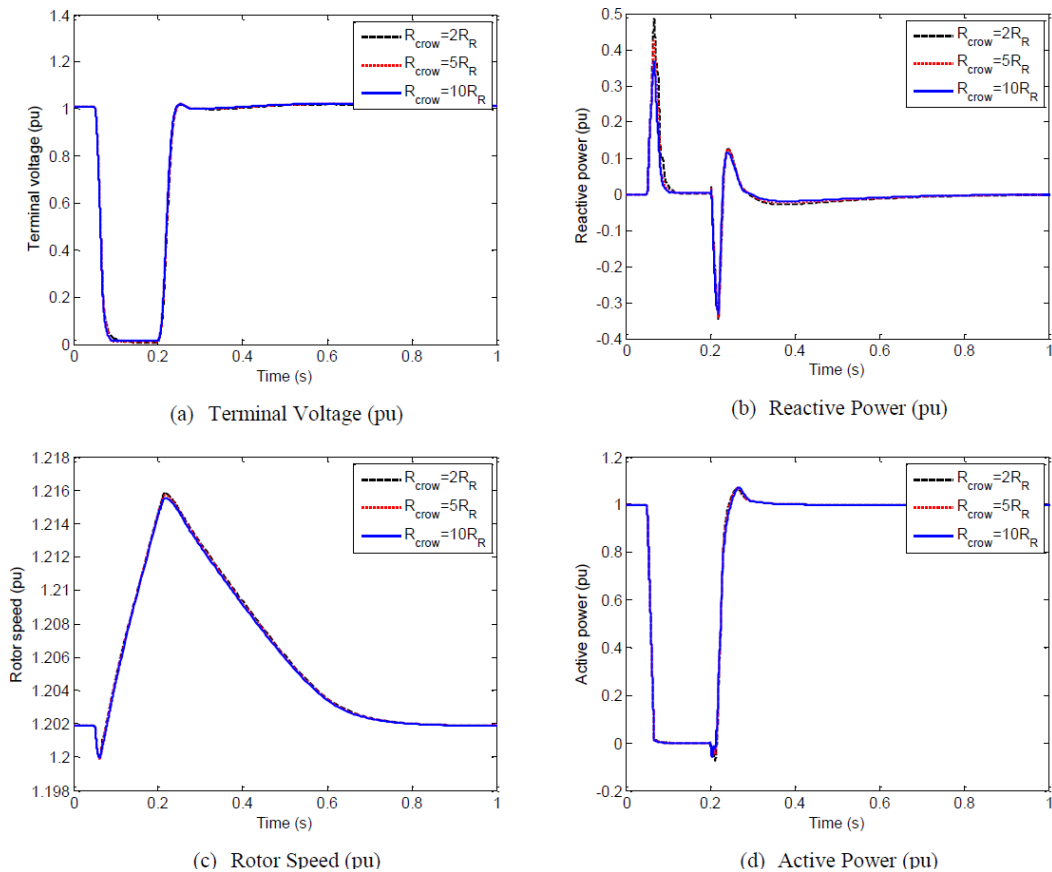


(a)  Terminal Voltage (pu)

(b)  Reactive Power (pu)

(c)  Rotor Speed (pu)

(d)  Active Power (pu)

**Figure 13:** Dynamic analysis of the DFIG for different resistance values of the crowbar system, during a 150 *ms* fault at Bus 7 (PCC) [SALL10].

### 4.2.2  Influence of the Operation Time of the Crowbar System

There are countries in which the TSO requires that reactive power is injected into the grid by the wind energy system during grid faults (for example Spain or Germany). In these cases the crowbar system must actuate for a shorter period of time to enable the RSC to realize the reactive power injection.

Figure 14 illustrates the behavior of the wind farm during a grid fault at Bus 5, for two different operation times of the crowbar system. The resistance value of the crowbar system is considered to be $R_{crow} = 2 \cdot R_R$. In order to maintain the voltage level at the

DC-link during the operation of the crowbar system, a DC-chopper (see Figure 2) is also activated.
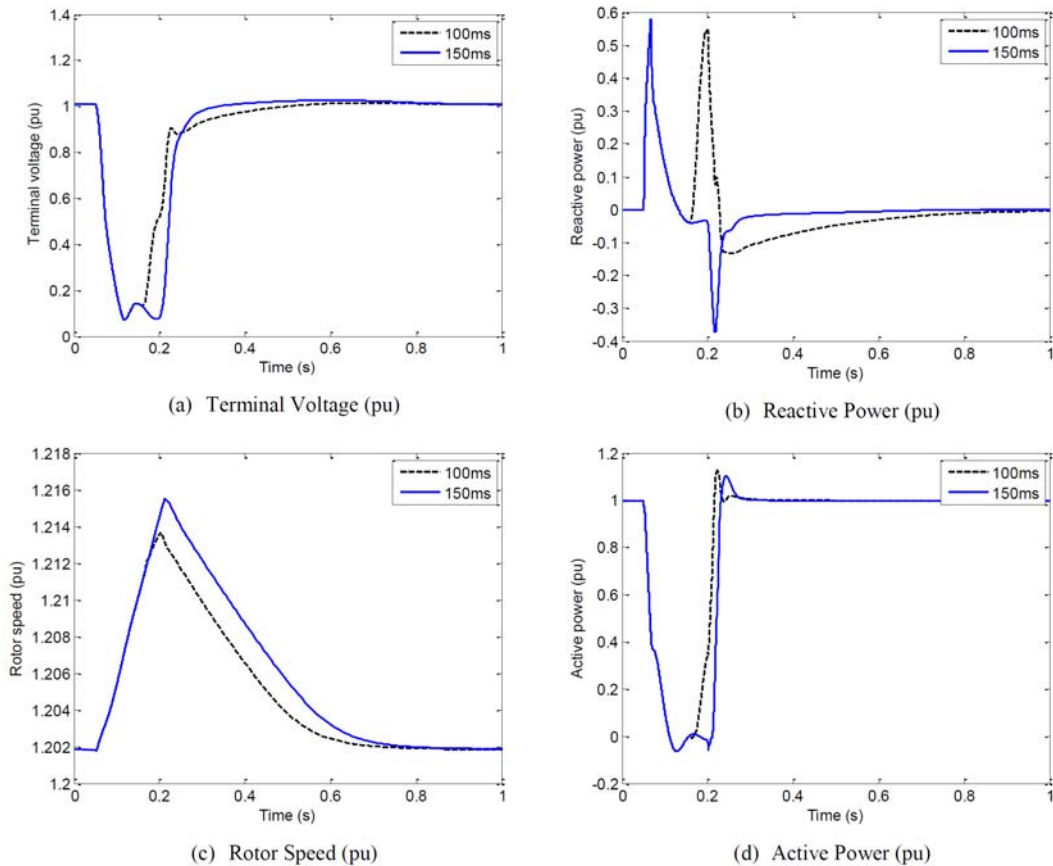


(a) Terminal Voltage (pu)

(b) Reactive Power (pu)

(c) Rotor Speed (pu)

(d) Active Power (pu)

**Figure 14:** Dynamic analysis of the DFIG for different operation times of the crowbar system, during a 150 *ms* fault at Bus 5 [SALL10].

For a 100 *ms* operation time of the crowbar system, the terminal voltage increases before the elimination of the grid fault (Figure 14a). This is due to the injection of reactive power by the RSC during the fault (Figure 14b, positive values). Operation at critical rotor speed is avoided for an operation time of 100 *ms*, for which the rotor speed has a lower value than for 150 *ms* (Figure 14c). The value of the injected active power is in both cases close to zero, since the terminal voltage is as well almost zero (Figure 14d) [SALL10].

The characteristics in case of a much more severe grid fault occurring close to the wind farm at the PCC (Bus 7) are shown in Figure 15. Similar to the previous investigated case, for an operation time of 100 *ms* the terminal voltage also increases before the elimination of the grid fault (Figure 15a). The reason is again the injection of reactive power by the RSC (Figure 15b, positive values). However, in this case the rotor speed reached for an operation time of 100 *ms* brings no significant changes in the performance when compared to an operation time of 150 *ms*, because the level of the injected reactive power is low for very low terminal voltage values (Figure 15c). Due to

the small terminal voltage levels the injected active power is again close to zero for both operation times (Figure 15d) [SALL10].
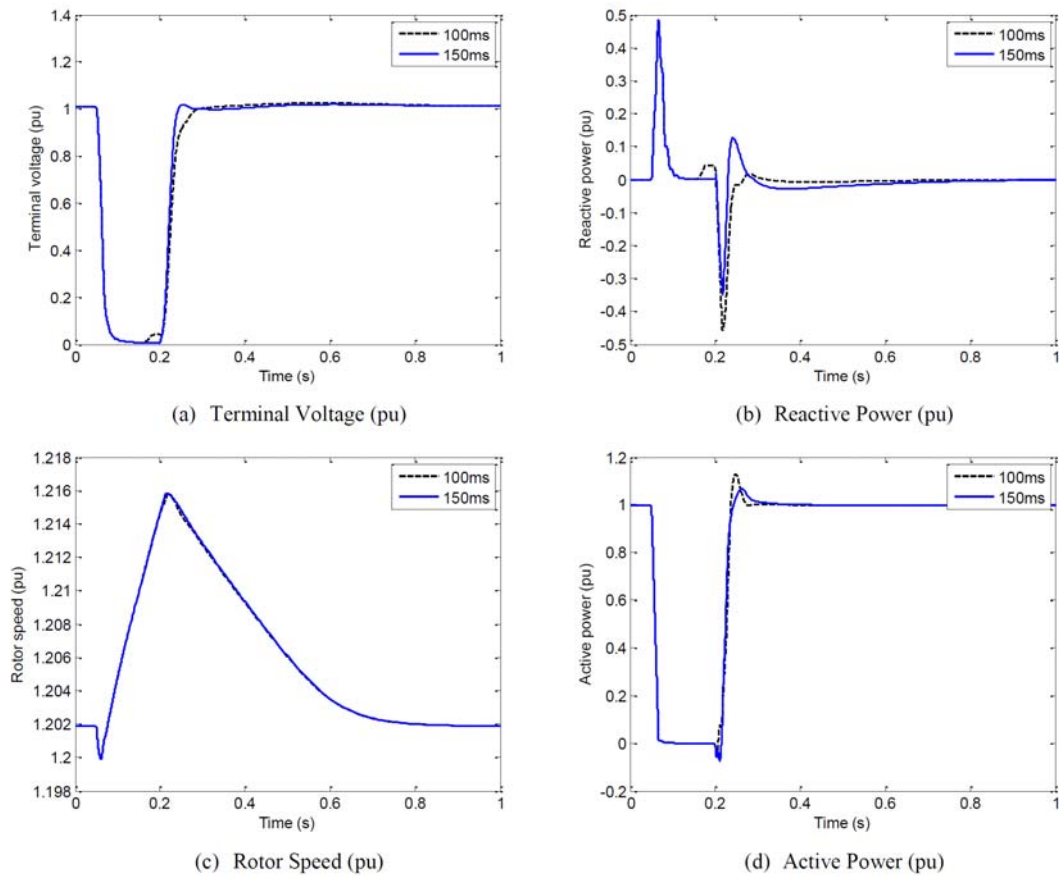


Figure 15: Dynamic analysis of the DFIG for different operation times of the crowbar system, during a 150 *ms* fault at Bus 7 (PCC) [SALL10].

Considering the two investigated grid faults, it can be seen that a shorter operation time of the crowbar system allows the injection of reactive power during a grid fault. However, this injection becomes limited for more severe faults.

# 5 Bearing currents and their mitigation in DFIG

Bearing currents are one of the main causes that lead to bearing failures in drive systems based on electrical motors or generators. There are two different types of bearing currents [MUET03]: bearing currents of line-operated electrical machines (also known as "classical" bearing currents) and inverter-induced bearing currents.

The "classical" bearing currents, a phenomenon which is well known, are a parasitic effect that mainly occurs due to the magnetic asymmetries in the electrical machine [ANDR67, BRAC90, SEIN69, SEIN92, WETH90]. These asymmetries lead to the formation of a parasitic AC magnetic flux linkage ($\phi_{parasitic}$) through the stator housing,

drive-end bearing, motor shaft and non drive-end bearing, which induces a voltage in these components. This shaft voltage ($v_{sh}$) can be measured between the two ends of the motor shaft (Figure 16).
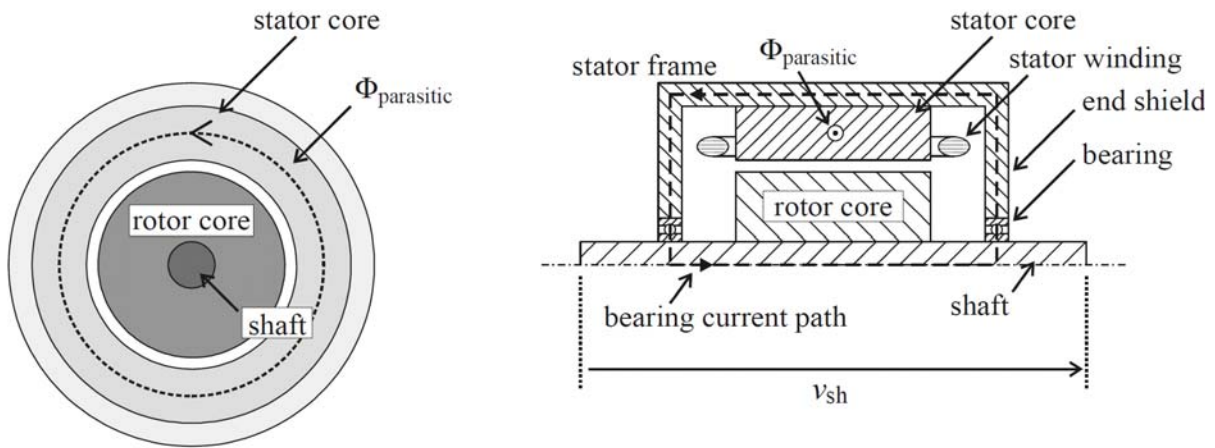


**Figure 16:** Bearing currents due to magnetic asymmetries in line-operated electrical machines [MUET03].

In wind energy systems based on DFIG the rotor windings are grid-connected via a back-to-back converter, in order to enable a decoupled control of active and reactive power. Such a power inverter works at very high frequency. There are many parasitic capacitive couplings between different components of the generator which may be neglected at low frequencies, but their influence is very important at high frequency. Due to the rapid development of power electronics technology, switching frequencies of the semiconductor elements have increased considerably. These fast switching transients ($dv/dt$) and the common mode voltage ($v_{com}$, defined as the arithmetic mean of the line-to-ground voltages of the three-phase system) can cause undesired effects in the electrical machines, the worst of which are the shaft to bearing voltage and the resulting inverter-induced bearing currents [ADAB09, MUET03], due to discharge machining effects. Four types of such currents can be distinguished (Figure 17): the first two relate to the influence of the common mode voltage on the bearing, the last two are caused by fundamental currents that result from the interaction of the common mode voltage with fast switching transients and the capacitive coupling between stator winding and motor frame.
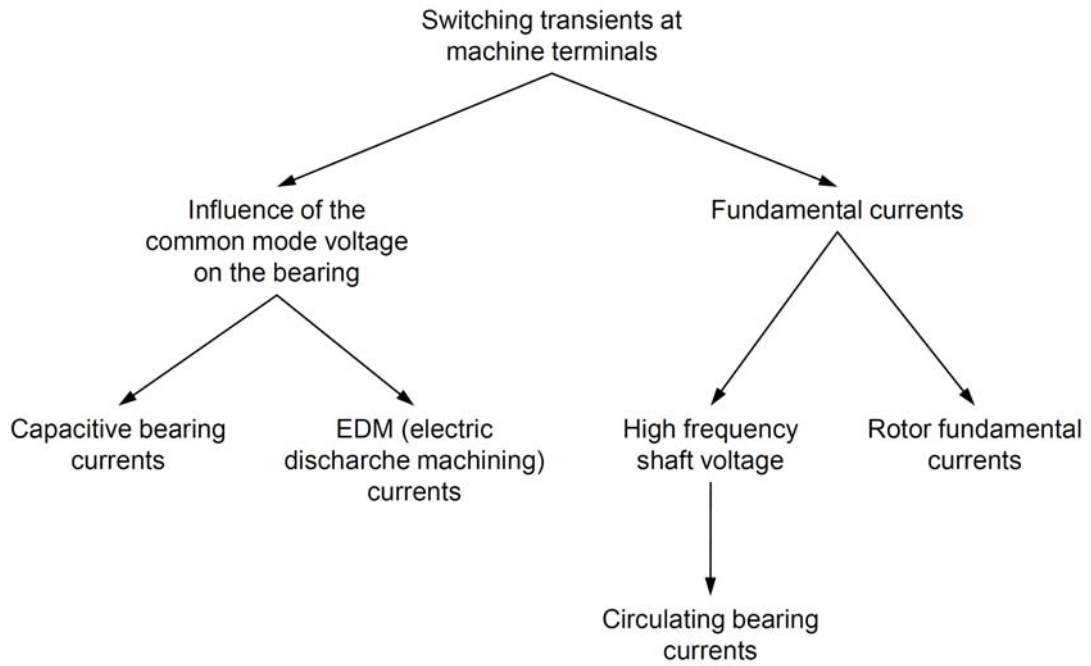
**Figure 17:** Types of inverter-induced bearing currents [MUET03].



**Figure 18:** Capacitive coupling in a DFIG (schematic front and side view) [ADAB09].

Figure 18 illustrates the existing parasitic capacitive couplings in a DFIG (schematic front and side view) between the stator winding and rotor ($C_{rs}$), the stator winding and stator frame ($C_{sf}$), the stator winding and rotor winding ($C_{ws}$), the stator frame and rotor ($C_{rf}$), the rotor winding and rotor ($C_{wr}$), the rotor winding and stator frame ($C_{wf}$) and the ball bearing and inner and outer races ($C_{b1}, C_{b2}$) [ADAB09, ADAB10].

The problematic issues concerning the performance of the DFIG power converters are the common mode voltages from both the rotor and the stator-side converter. According to the high frequency model of the DFIG shown in Figure 19, the shaft voltage can be calculated as [ADAB09, ADAB10]:

$$V_{shaft} = \frac{C_{wr}}{C_{wr} + C_{rf} + C_b + C_{sr}} \cdot V_{com,R} + \frac{C_{sr}}{C_{wr} + C_{rf} + C_b + C_{sr}} \cdot V_{com,S} =$$

(5)

$$= K_R \cdot V_{com,R} + K_S \cdot V_{com,S}$$

where $V_{com,R}$ and $V_{com,S}$ are the common mode voltages of the rotor and stator windings, and $K_R$ and $K_S$ are defined as the rotor and the stator-side capacitance factors, responsible for the total shaft voltage generation.
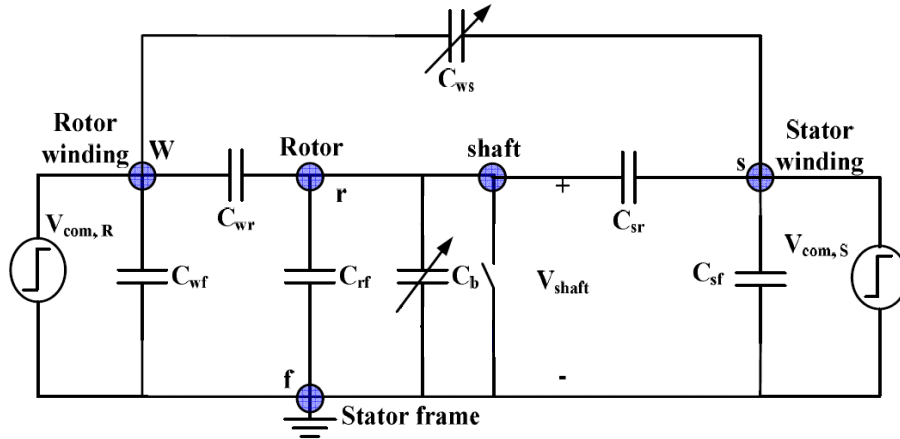


**Figure 19:** High frequency model of a DFIG [ADAB09].

According to [ADAB09] and [ADAB10] the most problematic capacitive coupling in a DFIG is the capacitive coupling between the rotor winding and the rotor frame, $C_{wr}$. If we consider that $C_{wr} >> C_{rf} + C_b + C_{sr}$, then the shaft voltage is determined by $C_{wr}$ ($K_R$ will be almost 1 and $K_S$ will have a very small value). Typical amplitudes for the common mode voltages of the DFIG converters ($V_{com,R}$, $V_{com,S}$) and for the shaft voltages ($K_R \cdot V_{com,R}$, $K_S \cdot V_{com,S}$, $V_{shaft}$) are illustrated in Figure 20. A time characteristic of the total shaft voltage is given in Figure 21. For these waveforms, the capacitive couplings have the following values: $C_{wr} = 5\,nF$, $C_{rf} = 0.6\,nF$, $C_{sr} = 0.3\,nF$ and $C_b = 0.1\,nF$ [ADAB09].
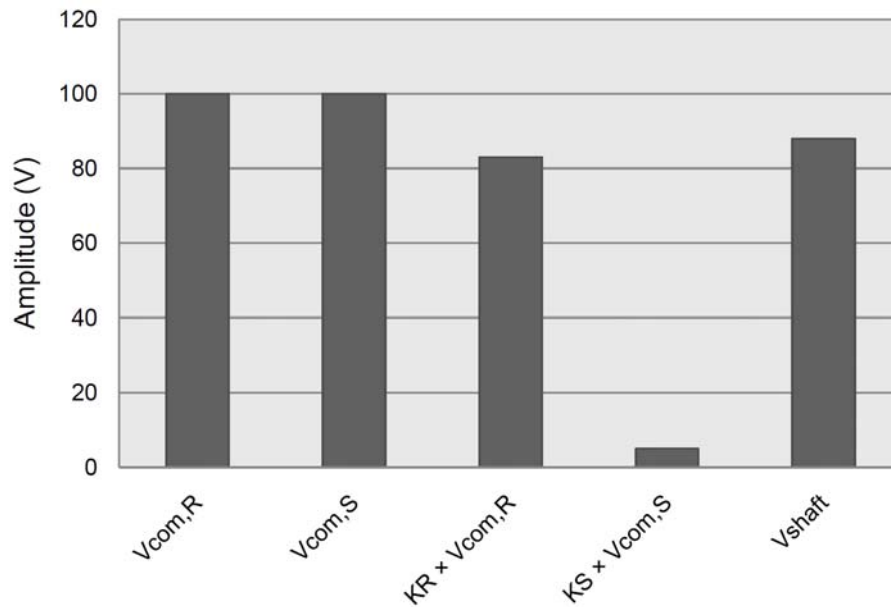
**Figure 20:** Typical amplitudes for the common mode voltages of the DFIG converters and for the shaft voltages.
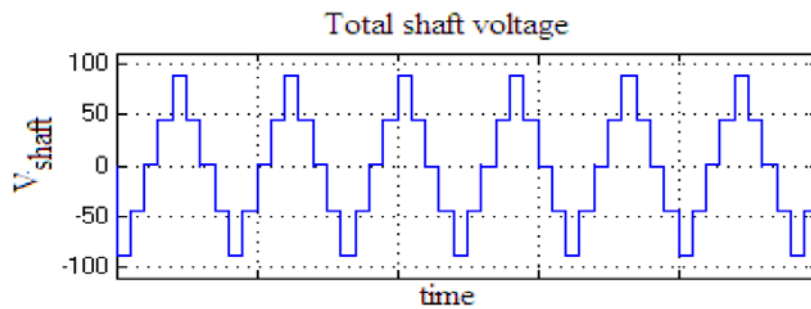


**Figure 21:** Time characteristic of the total shaft voltage [ADAB09].

Various shaft voltage mitigation techniques are given in the technical literature [ADAB09, ADAB10, GARC06, MUET03, ZITZ05], stating that a very important factor which should be considered is that the common mode voltage of the rotor-side converter contributes more to the shaft voltage when compared to the common mode voltage of the stator-side converter of a DFIG (see Figure 20). A reduced permittivity and an increased thickness of the insulation in the rotor slots are very efficient against shaft voltages. There are also different constructional parameters that can be changed in order to achieve the lowest possible shaft voltage due to the undesired capacitive couplings. Such parameters are for instance the stator slot tooth, the gap between slot tooth and winding, the height of the slot tooth and the air gap between rotor and stator. Considering such factors in an early stage of the DFIG design can reduce shaft voltages and thus high costs of resultant bearing current mitigation can be avoided [ADAB09, ADAB10].

Mitigation techniques can be grouped in two main categories [MUET03]: mitigation techniques on the inverter side and counter-measures against bearing currents on the generator side. On the inverter side shaft voltages can be reduced through inverter output filters ($dv/dt$ filters or reactors, sinusoidal filters etc.) and special voltage modulation techniques or common mode filters to reduce or eliminate common mode voltage. On the generator side counter-measures against bearing currents include insulated bearings, ceramic or hybrid bearings, insulated couplings, use of low impedance grease, rotor brushes and electrostatic shielding of the rotor. The effectiveness of these techniques is directly dependent to the type of bearing currents that are meant to be reduced or eliminated.

# 6 Conclusions

This paper presents the dynamic model and analysis of the DFIG based wind energy systems and offers a short insight into the problematic of bearing currents and their formation in such generators.

Three different control strategies of the DFIG rotor-side converter (RSC) and grid-side converter (GSC) for two types of grid faults have been analyzed in section 4.1. The grid faults occur at Bus 5 and Bus 7 (which is very close to the wind energy system terminals) in the test system shown in Figure 5, both for a time period of 150 $ms$. The characteristics presented in this section point out the need of an additional protection system in order to keep the wind energy system grid-connected during a severe fault (like the one that occurs at Bus 7). In this case the DC-link voltage levels exceed the acceptable limits, regardless of the implemented control strategy.

In section 4.2 the protection of the DFIG based wind energy system through the crowbar system and the influence of two different parameters of this system (resistance value and operation time) on the performance of the wind energy system have been presented. The shown characteristics indicate that the resistance values of the crowbar system have to be high enough to enable low reactive power consumption, when the wind energy system must remain grid-connected during faults. For more severe faults (close to the wind farm) the influence of the resistance values of the crowbar system is insignificant. In case of stricter grid code requirements (as for example in Germany or Spain) wind energy systems must inject reactive power into the grid. The operation time of the crowbar system must therefore be reduced to enable the RSC, which regulates the terminal voltage, to restart quickly. In this case the use of a DC-chopper is recommended.

The aspects discussed in section 4 of this paper indicate that the appropriate control strategy of the DFIG converters and the protection strategy during grid faults should be chosen by directly considering the grid code requirements imposed by the regional Transmission System Operator (TSO).

Section 5 of this paper describes the shaft voltage and the different types of resulting bearing currents, the inverter-induced bearing currents being the most critical type for power electronics operated electrical machines, such as the DFIG. The most critical factor for these currents is the parasitic capacitive coupling between the rotor winding and the rotor frame. This undesired phenomenon can be positively influenced by changing various design values of the generator. Also, depending on the type of bearing currents, various methods can be employed on the inverter or on the generator side, in order to reduce or eliminate these currents.

# 7 References

[ADAB09]   Adabi, J.; Zare, F.; Ghosh, A.; Lorenz, R.D.
           Analysis of Shaft Voltage in a Doubly-fed Induction Generator.
           In: International Conference on Renewable Energies and Power
           Quality – ICREPQ'09, Valencia, Spain, 2009.

[ADAB10]   Adabi, J.; Zare, F.; Ghosh, A.; Lorenz, R.D.
           Calculations of capacitive couplings in induction generators to analyse
           shaft voltage.
           In: IET Power Electronics, vol. 3, iss. 3, 2010, p.379-390.

[AKHM03]   Akhmatov, V.
           Analysis of Dynamic Behaviour of Electric Power Systems with Large
           Amount of Wind Power.
           PhD Thesis, TU Denmark, Denmark, 2003.

[ANDR67]   Andresen, E.
           Über Wellenspannungen bei Asynchronmaschinen mit ungeteilten
           Blechen (in German).
           In: Bulletin SEV 58, 1967, p. 839-844.

[BRAC90]   Brach, K.
           Wellenspannungen bei Drehstrom-Induktionsmaschinen mit
           Käfigläufer (in German).
           Dissertation Universität Hannover, 1990.
           In: VDI-Verlag, Reihe 21, Nr. 63.

[GARC06]   Garcia, A.M.; Holmes, D.G.; Lipo, T.A.
           Reduction of Bearing Currents in Doubly Fed Induction Generators.
           Industry Applications Conference, 41st IAS Annual Meeting.
           In: Conference Record of the 2006 IEEE, vol.1, 2006, p. 84-89.

[MUET03]   Muetze, A.
           Bearing Currents in Inverter-Fed AC Motors.
           PhD Thesis, TU Darmstadt, Darmstadt, 2003.

[SALL08]   Salles, M.B.C.; Hameyer, K.; Cardoso, J.R.; Freitas, W.
           Dynamic Analysis of Wind Turbines Considering New Grid Code
           Requirements.
           In: IEEE Proceedings of the 2008 International Conference on
           Electrical Machines – ICEM 2008, p. 1-6.

[SALL09]   Salles, M.B.C.; Cardoso, J.R.; Grilo, A.P.; Rahmann, C.; Hameyer, K.
Control Strategies of Doubly Fed Induction Generators to Support
Grid Voltage.
In: IEEE Proceedings of the 2009 International Electric Machines and
Drives Conference – IEMDC 2009, p. 1551-1556.

[SALL10]   Salles, M.B.C.; Hameyer, K.; Cardoso, J.R.; Grilo, A.P.; Rahmann, C.
Crowbar System in Doubly Fed Induction Wind Generators.
In: Energies, vol. 3, 2010, p. 1551-1556.

[SAUE98]   Sauer, P.W.; Pai, M.A.
Power System Dynamics and Stability.
In: Prentice Hall, Upper Saddle River, NJ, USA, 1998.

[SEIN69]   Seinsch, H.O.
Lagerströme bei Drehstrom-Induktionsmaschinen, Ursachen und
Methoden ihrer Unterdrückung (in German).
In: Conti Elektro-Berichte 15, 1969, p.43-51.

[SEIN92]   Seinsch, H.O.
Oberfelderscheinungen in Drehfeldmaschinen, Grundlagen zur
analytischen und numerischen Berechnung (in German).
In: B.G. Teubner, Stuttgart, 1992.

[SEMA06]   Seman, S.; Niiranen, J.; Arkkio, A.
Ride-Through Analysis of Doubly Fed Induction Wind-Power Generator
Under Unsymmetrical Network Disturbance.
In: IEEE Transactions on Power Systems, vol. 21, 2006, p. 1782-1789.

[SLOO03]   Slootweg, J.G.; Polinder, H.; Kling, W.L.
Representing Wind Turbine Electrical Generating Systems in
Fundamental Frequency Simulations.
In: IEEE Transactions on Energy Conversion, vol. 18, 2003, p.516-524.

[WETH90]   Weth, H.
Experimentelle und theoretische Untersuchung der Wellenspannungen
von Drehstrom-Asynchronmotoren bei Umrichterspeisung (in German).
In: European Conference on Power Electronics and Applications, 2005..

[ZITZ05]   Zitzelsberger, J.; Hofmann, W.; Wiese, A.
Bearing Currents in Doubly-Fed Induction Generators.
In: IEEE Transactions on Energy Conversion, vol. 18, 2003, p.516-524.